# High-Throughput Mapping of the Superconducting Phase Diagram Combining Composition-Spread $FeSe_{1-x}Te_x$ Film with Carrier Doping

Xuewei Wang[1,2], Changhong Yuan[1,2], Tianxiang Liu[1,2], Qiuyan Shi[1,2], Yating Jiang[1,2], Zhiyu Huang[1,2], Yutong Wang[1,2], Yuhan Jin[1,2], Xingyu Jiang[1], Beiyi Zhu[1], Jie Yuan[1], Zefeng Lin[1*], Qihong Chen[1*], and Kui Jin[1,2,3]

[1]*Beijing National Laboratory for Condensed Matter Physics, Institute of Physics, Chinese Academy of Sciences, Beijing 100190, China*
[2]*School of Physical Sciences, University of Chinese Academy of Sciences, Beijing 100049, China*
[3]*Songshan Lake Materials Laboratory, Dongguan 523808, China*

(Received 26 January 2026; accepted manuscript online 2 April 2026)

A high-throughput method is developed to investigate the superconducting phase diagram of combinatorial (composition-spread) $FeSe_{1-x}Te_x$ ($0 \leq x \leq 1$) films under electron doping. Composition-spread $FeSe_{1-x}Te_x$ films are fabricated on single $CaF_2$ substrates using combinatorial laser molecular beam epitaxy. An integrated device structure combining ionic-liquid gating with $FeSe_{1-x}Te_x$ films enables simultaneous transport measurements over the whole composition range. Electrochemical gating significantly enhances the superconducting transition temperature ($T_c$) in the Se-rich region, reaching values above 40 K. With increasing Te content, both the maximum $T_c$ and the gating efficiency gradually decrease. A comprehensive two-dimensional superconducting phase diagram is constructed as a function of Te content and doping level. These results establish an ideal approach for rapidly exploring the correlation between chemical composition, carrier doping, and superconductivity in Fe-based superconductors.

DOI: 10.1088/0256-307X/43/5/050707 CSTR: 32039.14.0256-307X.43.5.050707

*1. Introduction.* Iron-based superconductors, as a distinct class of high-temperature superconductors, have garnered significant attention due to their unconventional superconducting properties.[1–5] Among them, FeSe possesses the simplest layered structure within the iron-based superconductor family, making it a pivotal system for studying various phenomena such as the competition between orbital ordering and superconductivity, as well as potential topological superconducting behavior.[6–10] The superconducting transition temperature ($T_c$) of bulk FeSe single crystals is around 8 K under ambient pressure. Isovalent substitution of Se with Te in FeSe leads to lattice expansion, which can be regarded as chemical doping under negative chemical pressure.[11,12] FeTe shares a similar layered crystal structure with FeSe, yet exhibits markedly different electronic correlations.[13] Through chemical substitution of Te for Se in FeSe, $T_c$ exhibits a dome-like behavior: $T_c$ initially increases and then decreases with increasing Te doping level, reaching a maximum of approximately 15 K at a Te concentration of $\sim$0.5 in single crystals, or 20 K at a Te concentration of $\sim$0.3 in thin films.[14–16] Moreover, the composition phase diagram of the $FeSe_{1-x}Te_x$ ($x = 0 \sim 1$) system reveals rich physical properties. At the Te-rich region, long-range antiferromagnetism (AFM) emerges, reminiscent of the parent compounds of cuprate superconductors. As the Se content increases, this long-range AFM order is suppressed and superconductivity emerges. In the Se-rich region, pure nematic order without magnetism is observed.[14–16] Consequently, the $FeSe_{1-x}Te_x$ system is regarded as a promising platform for investigating the interplay among the superconducting state, nematic order, and AFM.

One of the most extraordinary properties of the FeSe system is its wide tunability of $T_c$ through various approaches. For instance, alkali-metal intercalation (e.g., $A_xFe_{2-y}Se_2$, $A$ = K, Rb, Cs)[17–19] and molecular intercalation [e.g., (Li, Fe)OHFeSe, $(TBA)_xFeSe$][20–22] have been shown to raise $T_c$ above 30 K. Remarkably, monolayer FeSe films epitaxially grown on $SrTiO_3$ substrates have demonstrated $T_c$ values exceeding 65 K.[23–26] Compared to bulk FeSe crystals, these $T_c$-enhanced systems exhibit pronounced electron doping effects, originating from charge transfer induced either by intercalation or from the oxide substrate to the FeSe layer. This suggests that electron doping plays a critical role in boosting the $T_c$ of FeSe. Field-effect transistor offers a precise and efficient approach to electron doping to tune the carrier concentration.[27] In particular, ionic liquid-based electric double-layer transistor (EDLT) has been widely employed in modulating superconducting properties, owing to its strong gating capability and structural simplicity.[28,29] Previous studies have reported that ionic liquid-gating via an EDLT can enhance the $T_c$ of FeSe up to 48 K.[30]

Overall, both Te substitution and electron doping

*Corresponding authors. Email: linzefeng@iphy.ac.cn; qihongchen@iphy.ac.cn

can significantly modify the Fermi surface topology and band structure of FeSe-based materials, thereby providing an excellent platform for studying the evolution of various ordered states and their interplay with superconductivity.[31,32] Although the effects of electron doping have been extensively studied in undoped FeSe, there are only limited reports on Te substitution for electron-doped FeSe.[33–35] In the few available studies, restricted to Te contents below $x \approx 0.5$, the maximum superconducting transition temperature $T_c$ under electron doping exhibits a pronounced suppression with increasing Te concentration.[34–36] To date, a complete phase diagram covering the entire Te doping range is still lacking, owing to the time-consuming experimental cycles required for individual single-composition samples, in which ionic liquid gating can be applied to only one composition at a time.

Recently, composition-spread $FeSe_{1-x}Te_x$ ($x = 0 \sim 1$) films grown by combinatorial laser molecular beam epitaxy (CLMBE) have successfully achieved a continuous variation of Te content on a single piece of sample.[15] This technique allows for more precise control over chemical composition. On this basis, combining ionic liquid gating with $FeSe_{1-x}Te_x$ composition-spread films would enable simultaneous gating of multiple compositions on a single sample. This approach will facilitate the construction of a complete ionic liquid-gating phase diagram for $FeSe_{1-x}Te_x$ and the investigation of the evolution of its superconducting properties in detail.

In this work, we employed CLMBE to grow composition-spread $FeSe_{1-x}Te_x$ ($x = 0 \sim 1$) films and designed a unique gating configuration with multiple resistivity channels by integrating ionic liquid gating onto the composition-spread film. The results show that applying a positive gate voltage to introduce electron doping leads to an enhancement of $T_c$ across a wide compositional range, with the maximum $T_c$ exceeding 40 K. As the Te content increases, the highest achievable $T_c$ gradually decreases, and the required gating conditions also become significantly more drastic. On this basis, a comprehensive superconducting phase diagram is established, which provides insights into the evolution of superconductivity in $FeSe_{1-x}Te_x$ as a function of electron doping. Our results provide a new electrostatic modulation method to efficiently study the evolution of superconducting properties in high-temperature superconductors.

*2. Experimental Methods.* Composition-spread $FeSe_{1-x}Te_x$ films were fabricated via CLMBE on (00$l$)-oriented $CaF_2$ single-crystal substrates with dimensions of $10 \times 10 \times 0.5\,mm^3$. The detailed growth process can be found in Ref. [15]. The resulting films exhibited continuous compositional variation from $x = 0$ to $x = 1$ over a spatial range of 8.4 mm, with a typical film thickness of approximately 100 nm, as shown in Fig. 1(a). The Te-composition gradient was designed to span 8.4 mm for two reasons. First, this avoids the substrate-edge regions, where the film may exhibit degraded quality compared to the interior area, and the edge area is more prone to damage during micro/nanofabrication processes. Second, it leaves

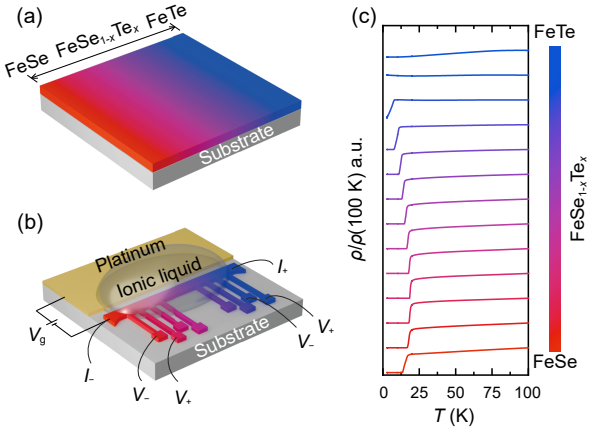


**Fig. 1.** (a) Schematic illustration of the composition-spread $FeSe_{1-x}Te_x$ ($x = 0 \sim 1$) films, where the red and blue regions represent the Se-rich and Te-rich regions, respectively, and the gray area denotes the $CaF_2$ substrate. (b) Schematic of the device structure combining ionic-liquid gating with the composition-spread film. The central main channel consists of the $FeSe_{1-x}Te_x$ film patterned by ion-beam etching; the yellow region corresponds to the Ti/Au gate electrode, and the overlying liquid is the ionic liquid DEME-TFSI. (c) Temperature dependence of the normalized resistivity curves at different Te doping levels from 0 to 1 before gating.

sufficient space on both sides for the current terminals used in the electrical transport measurements.

To facilitate electrical transport measurements, over 15 microbridges were patterned on the film surface using either UV photolithography or a predefined mask covering the substrates during growth, as illustrated in Fig. 1(b). Resistivity channels were primarily patterned on one side of the substrate, while the opposite side was later coated with a Ti/Au layer via electron beam evaporation, which functioned as a gate electrode for subsequent ionic liquid gating. Samples were mounted on the measurement stage using N-grease, and indium soldering was used to make electrical contacts. Four-probe resistance measurements were performed using a Keithley 6221 current source (typical current $\sim 100\,\mu A$) and a Keithley 2182 nanovoltmeter. A Keithley 3706A switch matrix enabled the simultaneous measurement of 15 resistance channels. All electrical transport measurements were conducted in a cryogen-free measurement system (CFMS, Cryogenic Ltd.).

Before measurements, the ionic liquid DEME-TFSI [N, N-diethyl-N-(2-methoxyethyl)-N-methylammonium bis-(trifluoromethylsulfonyl)imide] was dropped to bridge the gate electrode and the active channel region. The gate and source electrodes were connected to a Keithley 2450 source meter, which was used to apply the gate voltage ($V_g$) and monitor the gate leakage current during gating. During the gating process, the degree of ionic injection was primarily controlled by adjusting the gate voltage ($V_g$), gating temperature ($T_g$), and gating time ($t_g$). The general experimental procedure was as follows: a predefined gate voltage $V_g$ was first applied at a temperature below the freezing point of the ionic liquid (approximately 180 K). The system was then gradually heated to the target gating temperature $T_g$ while monitoring the gate

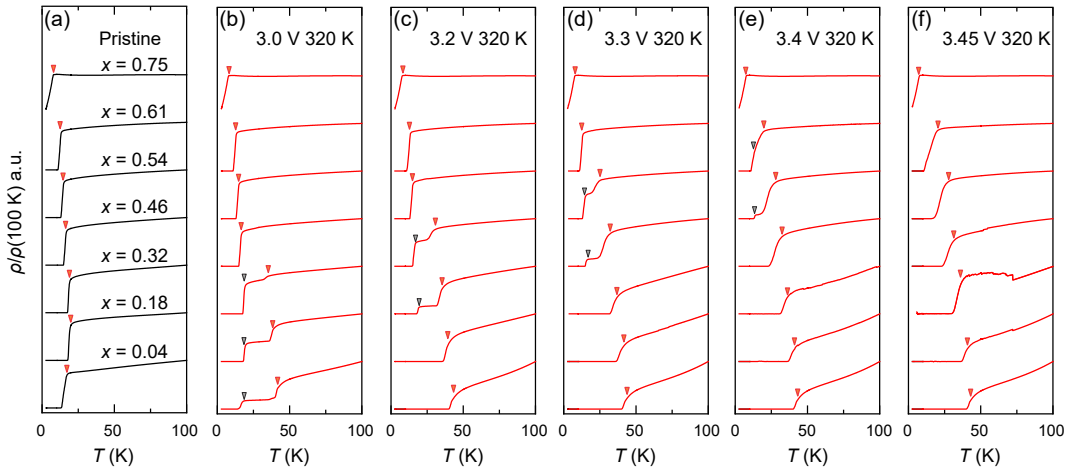


**Fig. 2.** Temperature-dependent resistivity of selected compositions under various gating conditions. (a) Initial state without gating; (b)–(f) Evolution of resistivity versus temperature as the gate voltage $V_g$ increases from 3.0 V to 3.45 V for corresponding Te contents. Specifically, the gray arrows denote the lower $T_c$ associated with a two-step transition observed during the gating process, whereas the orange arrows indicate the highest $T_c$ attained after gating.

leakage current. After maintaining this condition for a duration $t_g$, the sample was cooled down for measurements to evaluate the change in $T_c$, which was used to guide subsequent gating conditions. Considering that the optimal gating conditions vary across compositions, multiple rounds of tuning were required on a single sample to achieve the maximum $T_c$ for each composition.

*3. Results and Discussion.* As shown in Fig. 1(b), approximately 15 pairs of electrodes were patterned for resistance measurements, with an inter-electrode spacing of $\sim$460 µm. The relative change in Te content between adjacent channels is approximately 0.06, which is represented in terms of the Te substitution ratio. Figure 1(c) presents the temperature-dependent resistivity ($R$–$T$) curves (2.5–100 K) on the as-grown composition-spread film spanning from the FeSe end to the FeTe end. Clear superconducting transitions are observed for compositions with Te content in the range of 0 to 0.9. As the Te content increases, the superconducting transition temperature $T_c$ exhibits a dome-like dependence, which is consistent with previously reported phase diagrams of $FeSe_{1-x}Te_x$ films.[15,16] Here, $T_c$ is defined as the intersection point between the extrapolated superconducting transition line and the extrapolated normal-state resistivity line.

Subsequently, we carried out ionic liquid gating experiments on the composition-spread films. Under identical gating conditions, different compositional regions exhibited distinct gating responses. Figure 2 presents representative temperature-dependent resistivity curves for several selected compositions: $x$ = 0.04, 0.18, 0.32, 0.46, 0.54, 0.61, and 0.75. Figure 2(a) shows the initial (ungated) resistivity-temperature curves for these compositions. The gating conditions were adjusted based on the degree of resistivity change in the normal state; these gating parameters may vary slightly across samples. Under relatively mild gating conditions ($V_g$ = 3.0 V, $T_g$ = 320 K, with a typical gating time $t_g \sim$ 7200 s), channels closer to the Se-rich region ($x$ = 0.04, 0.18) exhibited a clear enhancement of $T_c$, as shown in Fig. 2(b). However, a two-step transition was observed, indicating the presence of distinct superconducting components in the film. This similar inhomogeneous modulation phenomenon has also been reported in previous studies on ionic liquid-gated bulk FeSe.[37] For other compositions with higher Te content, negligible change in $T_c$ was observed under the same gating conditions.

As shown in Fig. 2(c), with the gating voltage increasing to $V_g$ = 3.2 V at $T_g$ = 320 K, the Se-rich region ($x$ = 0.04, 0.18) approached the optimal gating modulation, with $T_c$ values rising above 40 K. Channels with intermediate Te content ($x$ = 0.32, 0.46) began to show similar two-step superconducting transitions. Figures 2(d) and 2(e) display the resistivity curves under higher gating voltages ($V_g$ = 3.3 V and 3.4 V, $T_g$ = 320 K), where all channels with Te content below 0.7 exhibited $T_c$ enhancement. The highest $T_c$ values showed a decreasing trend with increasing Te content. In contrast, for the channels with higher Te content ($x$ = 0.75), the resistive behavior remained virtually unchanged before and after gating, even under the highest applied gating conditions ($V_g$ = 3.45 V, $T_g$ = 320 K), as shown in Fig. 2(f). The maximum gate voltage applied here was chosen to avoid electrochemical reactions induced by the ionic liquid. It can be clearly seen that, under the gating voltage of 3.45 V, the channel near $x$ = 0.32 has already exhibited noticeable fluctuations in the resistance curve. Further increasing the gating voltage ($V_g$ = 3.52 V, $T_g$ = 320 K) led to sample degradation in certain compositional regions; e.g., the FeSe end channels exhibited a decrease in $T_c$, which is associated with sample degradation. Nevertheless, the $T_c$ of the FeTe end channels did not show notable change under the same gating conditions.

Subsequently, we extracted the $R$–$T$ curves corresponding to the optimal $T_c$ values achieved through ionic liquid gating for each composition. Figures 3(a)–3(f) present the $R$–$T$ curves (2.5–100 K) before and after gating for $FeSe_{1-x}Te_x$ samples with Te contents of $x$ = 0.04, 0.18, 0.32, 0.46, 0.61, and 0.75. For compositions near

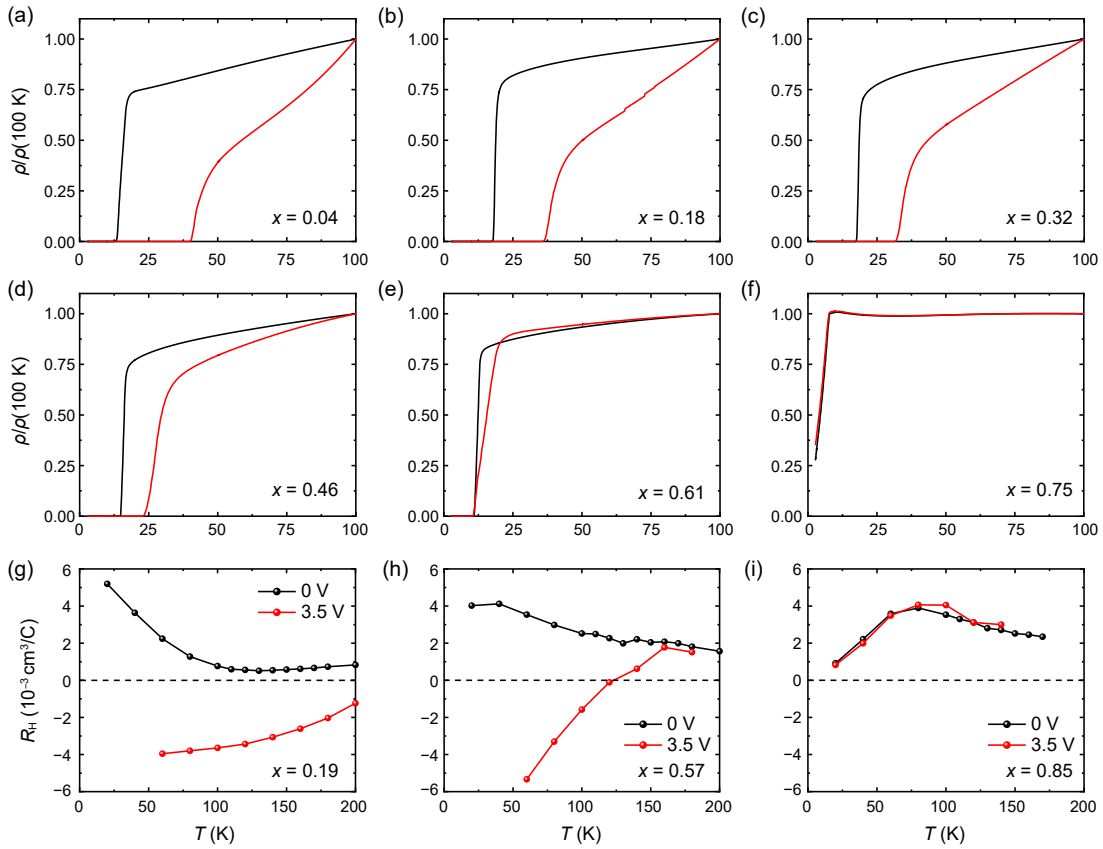


**Fig. 3.** (a)–(f) Temperature-dependent resistivity curves of $FeSe_{1-x}Te_x$ with different compositions before and after ionic-liquid gating. The black curves before gating were measured under identical conditions without the application of ionic liquid. The red curves after gating were obtained under the optimal gating conditions for each composition, defined as the point at which $T_c$ first reaches its maximum. (g)–(i) Temperature dependence of the Hall coefficient $R_H$ measured in the pristine state ($V_g = 0$ V) and the ion-gated state ($V_g = 3.5$ V), for three different compositions: $x = 0.19$, 0.57, and 0.85.

the Se-rich region, such as $x = 0.04$ in Fig. 3(a), $T_c$ exceeds 40 K even under relatively mild gating conditions ($V_g = 3.1$ V, ($T_g = 320$ K), consistent with previous studies on single-composition FeSe films.[30,38] As the Te content increases, the maximum $T_c$ gradually decreases, from 44 K ($x = 0.04$) to 41.4 K ($x = 0.18$), 38 K ($x = 0.32$), and 31.5 K ($x = 0.46$), as shown in Figs. 3(b)–3(d). Correspondingly, the required gate voltage increases to $V_g =$ 3.2 V, 3.3 V, and 3.4 V for $x = 0.18$, 0.32, and 0.46, respectively, with the gating temperature $T_g$ fixed at 320 K. For compositions with Te content above 0.5, $T_c$ after gating rapidly decreases with increasing Te content and eventually becomes insensitive to further modulation. Even under stronger gating conditions, samples near $x = 0.6$ exhibit only a slight enhancement in the onset temperature ($T_c^{onset}$), with little change in the zero-resistance transition, as shown in Fig. 3(e). For samples with higher Te content ($x = 0.75$), no significant enhancement of superconductivity is observed after gating; $T_c$ remains nearly unchanged or even shows a slight decrease, as shown in Fig. 3(f). Meanwhile, for channels with Te content below 0.6, a significant increase in room-temperature normal-state resistance was observed after gating, accompanied by a decrease in the normal-state resistance just above the superconducting transition. As a result, the residual resistivity ratio (RRR) increased following gating, which is consistent with previous reports on ionic liquid gating and serves as a clear signature of effective ion injection.[38] In contrast, the RRR of channels with Te content over 0.6 shows almost no change before and after gating, which may indicate that the effect of electron doping is weak in this range.

The effective doping and carrier concentration can be inferred from the evolution of the Hall coefficient ($R_H$), and thus we carried out Hall measurements on a composition-spread $FeSe_{1-x}Te_x$ film under ionic-liquid gating. Figures 3(g)–3(i) show the temperature dependence of $R_H$ before and after gating for three representative compositions: $x = 0.19$, 0.57, and 0.85. For the channel close to the FeSe end ($x = 0.19$), $R_H$ exhibits a pronounced temperature dependence before gating, signifying the complex competition between electron and hole pockets on the Fermi surface. The positive $R_H$ in the low-temperature limit indicates that transport is dominated by hole carriers at low temperatures. After gating ($V_g = 3.5$ V), $T_c$ is enhanced to above 40 K, and $R_H$ becomes negative over the entire measured temperature range and shows only weak temperature dependence. Particularly, it is nearly temperature independent at low temperatures, as shown in Fig. 3(g), suggesting a change in Fermi surface topology—from the

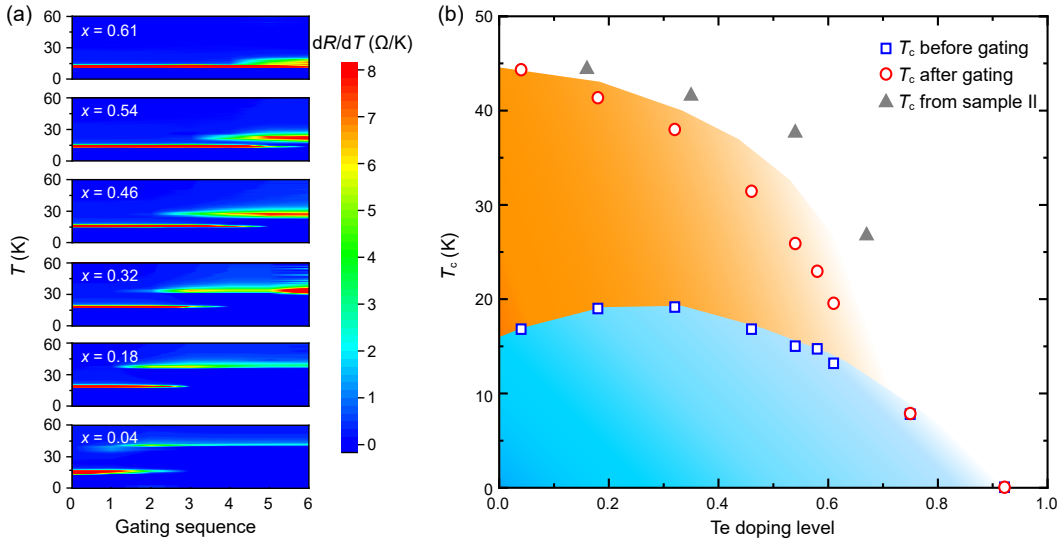


**Fig. 4.** (a) The two-dimensional phase diagram of differential resistance ranging from 0 to 60 K as a function of gating sequence, which shows the evolution of the superconducting transition for samples with different Te compositions under various gating conditions. The horizontal axis represents the gating sequence under the following conditions: 0 (pristine); 1 ($V_g$ = 3.0 V, $T_g$ = 310 K); 2 ($V_g$ = 3.0 V, $T_g$ = 320 K); 3 ($V_g$ = 3.2 V, $T_g$ = 320 K); 4 ($V_g$ = 3.3 V, $T_g$ = 320 K); 5 ($V_g$ = 3.4 V, $T_g$ = 320 K); 6 ($V_g$ = 3.45 V, $T_g$ = 320 K). The resistance data are taken from the curves in Fig. 2. (b) The phase diagram of $T_c$ and Te doping level ($x$). The blue hollow squares refer to the values of $T_c$ for the composition-spread $FeSe_{1-x}Te_x$ film before gating, while the red hollow circles refer to the highest $T_c$ achieved for each composition after gating, as extracted from Fig. 3. All the data presented in the above phase diagrams were obtained from one composition-spread film. The gray triangles correspond to ionic-liquid-gated sample II. The Te doping level shown in the phase diagram was estimated based on the relative position of the measurement channel on the composition-spread film.

coexistence of electron and hole pockets to electron pockets only—upon electron doping.[31,39] This behavior is consistent with previous Hall measurements on single-composition FeSe under ionic-liquid gating.[30,37,38] For the channel with Te content $x = 0.57$, $R_H$ increases slightly with cooling and remains positive throughout the entire measured temperature range before gating, as shown in Fig. 3(h). After ionic-liquid gating, $R_H$ changes from positive to negative as temperature decreases and remains negative in the low-temperature region. This indicates that this compositional channel also exhibits a pronounced electron-doping effect under gating. As Te content increases to $x = 0.85$ in Fig. 3(i), $R_H$ remains positive and exhibits no notable change, suggestive of a negligible electron-doping effect in this compositional range. Overall, the electron-doping effect progressively weakens with increasing Te content under the same gating conditions.

Experimentally, under the same conditions, electron doping is realized much more readily near the FeSe end than on the FeTe side. Since electron doping is achieved via ion injection, the higher-Te compositions appear more resistant to degradation because ion intercalation is strongly suppressed. Fundamentally, why ion injection is easier on FeSe and more difficult on FeTe remains elusive. Several factors may contribute. First, the larger atomic radius of Te leads to a thicker Fe-Te layer and modified interlayer geometry, which may reduce diffusion pathways and increase the ion diffusion barrier. Second, defects may be important. FeTe commonly contains interstitial Fe, which can occupy positions that might otherwise serve as ion diffusion channels, and therefore hinder ion migration.[40,41] Third, the electrochemical reaction energetics may differ. FeSe hosts rich intercalation chemistry, including alkali-metal-intercalated[17,18] and molecule-intercalated[20,22] superconducting phases, whereas comparable stable intercalated superconductors based on FeTe have rarely been reported. These experimental facts suggest the formation energy for intercalation of FeTe is significantly higher, and the electrochemical driving force in our experiment may be insufficient to realize effective doping.

Based on the transport measurements, figure 4(a) summarizes the evolution of derivative resistivity $dR/dT$ with gating sequence for various Te compositions. The vertical axis qualitatively reflects the evolution of $T_c$ before and after gating for the Te contents of $x = 0.04$, 0.18, 0.32, 0.46, 0.54, and 0.61 from bottom to top. For compositions with gate-tunable $T_c$, the transition progresses through three typical stages: a low-$T_c$ state, an intermediate regime with coexisting distinct $T_c$ values, and a high-$T_c$ state. After reaching the optimal gating state for each composition, $T_c$ remains essentially unchanged until degradation occurs due to ionic-liquid-induced corrosion. Moreover, as Te content increases, a higher gate voltage is required to induce noticeable changes in $T_c$, indicating that increased Te doping significantly raises the threshold for effective ion injection. It should also be noted that gating sequence on the horizontal axis serves only as an approximate indicator of the extent of doping concentration.[37]

We extracted the $T_c$ values before and after gating

and constructed a two-dimensional $T_c$–$x$ phase diagram, as shown in Fig. 4(b). Before gating, $T_c$ increases from approximately 16 K near the Se-rich region to nearly 20 K around a Te content of $\sim$0.3 and subsequently decreases with further Te substitution until the superconducting transition vanishes, as indicated by the blue hollow squares in Fig. 4(b). This trend is consistent with previously reported results, confirming the high quality of the composition-spread $FeSe_{1-x}Te_x$ films.[15] After ionic-liquid gating, the highest $T_c$ achieved for each composition under its respective optimal gating conditions was extracted and summarized in Fig. 4(b). At the Se-rich region, the highest $T_c$ after gating exceeds 40 K, reaching levels comparable to those reported for single-composition FeSe films under similar gating conditions.[30] As the Te content increases, the highest $T_c$ after gating gradually decreases, and the decreasing trend becomes more pronounced. The same gating experiment was repeated on sample II, and the resulting $T_c$ values are represented by the gray triangles in Fig. 4(b). These samples also exhibited similar $T_c$ evolution after gating, while the $T_c$ uncertainty may be attributed to differences in the actual Fe content of the films, which may vary slightly from sample to sample.[15]

It has been well known that nematic fluctuations may promote superconductivity in the pristine $FeSe_{1-x}Te_x$ system,[42,43] which was highlighted by recent nuclear magnetic resonance studies.[44] However, for electron-doped $FeSe_{1-x}Te_x$, no pronounced resistivity kink, which signifies the electronic nematic transition, has been observed in the $R$–$T$ curves after gating, both in our work and in previous studies.[30,39,45] Angle-resolved photoemission spectroscopy (ARPES) studies have also demonstrated that nematic order in FeSe is significantly suppressed upon electron doping.[31,46] Different from the dome-shaped superconducting phase, which may be related to nematic fluctuations in the $FeSe_{1-x}Te_x$ system before gating,[43] the maximum $T_c$ achieved after gating decreases monotonically with increasing Te content, without any anomaly across the nematic critical point. This suggests that the underlying mechanism is fundamentally different before and after electron doping.

Although FeSe and FeTe share a similar layered crystal structure, they exhibit notable differences in electronic correlations and band structure. ARPES measurements have shown that, on the FeSe end, well-defined electron bands are present at the $M$ point of the Fermi surface, accompanied by moderate electronic correlations.[32] As the Te content increases ($x > 0.5$), the electronic bands are heavily renormalized, indicating the emergence of strong electronic correlations in this doping regime, and the electron pocket around the $M$ point becomes ill defined.[13,47] In FeSe samples, the expanded electron pocket at the $M$ point after electron doping plays a dominant role in transport.[31,39,48] In contrast, for samples with higher Te content, electron-correlation effects may induce a gap or strongly suppress the spectral weight in the ill-defined electron pockets under electron doping, thereby weakening the dominant contribution of the electron bands to transport.[33] Therefore, it is speculated that the observed decrease in the highest $T_c$ after gating with increasing Te content may be related to changes in electronic correlations and band structure.

On the other hand, FeSe and FeTe also exhibit substantial differences in their magnetic properties. Previous studies have shown that the FeSe side does not host long-range antiferromagnetic order but only short-range antiferromagnetic fluctuations, which may mediate superconducting pairing.[49–51] In contrast, the FeTe side exhibits long-range antiferromagnetic order that competes with superconductivity.[52] Therefore, across the evolution from FeSe to FeTe, both the type and strength of the antiferromagnetic fluctuations change.[53,54] In particular, the composition where $T_c$ starts to decrease rapidly resides close to the onset of antiferromagnetic order, leading to the speculation that antiferromagnetic fluctuations play a dominant role in shaping the phase diagram of $FeSe_{1-x}Te_x$ after electron doping.

Unfortunately, carrier doping becomes very weak when approaching the FeTe end; thus, the electron-doping effect inside the antiferromagnetic order remains obscure. Future work combining gating experiments with magnetic and electronic structure measurements, together with relevant theoretical calculations, is required to further clarify why carrier doping is difficult to realize in this compositional range. With optimized gating configurations and protocols, more in-depth experiments near the FeTe end may reveal critical insights regarding the nature of superconductivity in Fe(Se, Te). To this end, our high-throughput experimental approach provides a robust foundation for such a comprehensive investigation of the interplay between electron doping, electronic structure, magnetism, and superconductivity in iron chalcogenides.

*4. Conclusion.* In summary, we have established a new gating device structure that combines composition-spread $FeSe_{1-x}Te_x$ ($x = 0 \sim 1$) films with ionic-liquid gating. It can efficiently achieve continuous and systematic gating across the entire compositional range within a single sample. By extracting the $T_c$ values of each composition under its optimal gating condition, a complete gating phase diagram of $FeSe_{1-x}Te_x$ was constructed. This gating configuration offers significant advantages over conventional single-composition gating techniques, which typically require multiple samples and extended gating times. The proposed device structure not only accelerates the establishment and exploration of a three-dimensional ($T_c$, Te content, electron doping) phase diagram but also provides a versatile method applicable to a broad class of high-throughput material systems.

*Acknowledgements.* This work was supported by the National Key R&D Program of China (Grant Nos. 2022YFA1403900, 2022YFA1403000, 2021YFA0718700, and 2022YFA1603900), the National Natural Science Foundation of China (Grant Nos. 12504169, 12374141, 12225412, and 52588301), the Chinese Academy of Sciences (CAS) President's International Fellowship Initiative (Grant Nos. 2024DM0018 and 2025PG0007), the CAS Project for Young Scientists in Basic Research (Grant

No. 2022YSBR-048), and the Open Research Fund of the Pulsed High Magnetic Field Facility, Huazhong University of Science and Technology (Grant No. WHMFC-2024001). This work is also technically supported by the Synergetic Extreme Condition User Facility (SECUF, https://cstr.cn/31123.02.SECUF).

## References

[1] Yoichi K, Hidenori H, Masahiro H, Ryuto K, Hiroshi Y, Toshio K, and Hideo H 2006 *J. Am. Chem. Soc.* **128** 10012
[2] Yoichi K, Takumi W, Masahiro H, and Hideo H 2008 *J. Am. Chem. Soc.* **130** 3296
[3] Chen X H, Dai P C, Feng D L, Xiang T, and Zhang F C 2014 *Natl. Sci. Rev.* **1** 371
[4] Li Y, Wu D, Shu Y, Liu B, Stuhr U, Deng G, Stampfl A P J, Zhao L, Zhou X, Li S, Pokhriyal A, Ghosh H, Hong W, and Luo H 2025 *Chin. Phys. Lett.* **42** 067405
[5] Zhang Y F, Zhang S N, Liu J X, Yang F, Li C S, Li J F, and Zhang P X 2024 *Chin. Phys. Lett.* **41** 117402
[6] Bohmer A E and Kreisel A 2018 *J. Phys.: Condens. Matter* **30** 023001
[7] Kreisel A, Hirschfeld P, and Andersen B 2020 *Symmetry* **12** 1402
[8] Hsu F C, Luo J Y, Yeh K W, Chen T K, Huang T W, Wu P M, Lee Y C, Huang Y L, Chu Y Y, Yan D C, and Wu M K 2008 *Proc. Natl. Acad. Sci. U.S.A.* **105** 14262
[9] Wang H, Cheng Z, Shi M, Ma D, Zhuo W, Xi C, Wu T, Ying J, and Chen X 2021 *Sci. China Phys. Mech. Astron.* **64** 287411
[10] Maeda A, Kobayashi T, and Nabeshima F 2026 *Supercond. Sci. Technol.* **39** 023001
[11] Yeh K W, Huang T W, Huang Y L, Chen T K, Hsu F C, M. Wu P, Lee Y C, Chu Y Y, Chen C L, Luo J Y, Yan D C, and Wu M K 2008 *EPL* **84** 37002
[12] Fang M H, Pham H M, Qian B, Liu T J, Vehstedt E K, Liu Y, Spinu L, and Mao Z Q 2008 *Phys. Rev. B* **78** 224503
[13] Tamai A, Ganin A Y, Rozbicki E, Bacsa J, Meevasana W, King P D, Caffio M, Schaub R, Margadonna S, Prassides K, Rosseinsky M J, and Baumberger F 2010 *Phys. Rev. Lett.* **104** 097002
[14] Imai Y, Sawada Y, Nabeshima F, and Maeda A 2015 *Proc. Natl. Acad. Sci. U.S.A.* **112** 1937
[15] Lin Z F, Tu S J, Xu J, Shi Y, Zhu B Y, Dong C, Yuan J, Dong X L, Chen Q H, Li Y M, Jin K, and Zhao Z Z 2022 *Sci. Bull.* **67** 1443
[16] Zhuang J, Yeoh W K, Cui X, Xu X, Du Y, Shi Z, Ringer S P, Wang X, and Dou S X 2014 *Sci. Rep.* **4** 7273
[17] Guo J, Jin S, Wang G, Wang S, Zhu K, Zhou T, He M, and Chen X 2010 *Phys. Rev. B* **82** 180520
[18] Wang A F, Ying J J, Yan Y J, Liu R H, Luo X G, Li Z Y, Wang X F, Zhang M, Ye G J, Cheng P, Xiang Z J, and Chen X H 2011 *Phys. Rev. B* **83** 060512
[19] Ying J J, Wang X F, Luo X G, Wang A F, Zhang M, Yan Y J, Xiang Z J, Liu R H, Cheng P, Ye G J, and Chen X H 2011 *Phys. Rev. B* **83** 212502
[20] Lu X F, Wang N Z, Wu H, Wu Y P, Zhao D, Zeng X Z, Luo X G, Wu T, Bao W, Zhang G H, Huang F Q, Huang Q Z, and Chen X H 2015 *Nat. Mater.* **14** 325
[21] Shi M Z, Wang N Z, Lei B, Ying J J, Zhu C S, Sun Z L, Cui J H, Meng F B, Shang C, Ma L K, and Chen X H 2018 *New J. Phys.* **20** 123007
[22] Sun R J, Quan Y, Jin S F, Huang Q Z, Wu H, Zhao L, Gu L, Yin Z P, and Chen X L 2018 *Phys. Rev. B* **98** 214508
[23] Wang Q Y, Li Z, Zhang W H, Zhang Z C, Zhang J S, Li W, Ding H, Ou Y B, Deng P, Chang K, Wen J, Song C L, He K, Jia J F, Ji S H, Wang Y Y, Wang L L, Chen X, Ma X C, and Xue Q K 2012 *Chin. Phys. Lett.* **29** 037402
[24] He S, He J, Zhang W, Zhao L, Liu D, Liu X, Mou D, Ou Y B, Wang Q Y, Li Z, Wang L, Peng Y, Liu Y, Chen C, Yu L, Liu G, Dong X, Zhang J, Chen C, Xu Z, Chen X, Ma X, Xue Q, and Zhou X J 2013 *Nat. Mater.* **12** 605
[25] Tan S, Zhang Y, Xia M, Ye Z, Chen F, Xie X, Peng R, Xu D, Fan Q, Xu H, Jiang J, Zhang T, Lai X, Xiang T, Hu J, Xie B, and Feng D 2013 *Nat. Mater.* **12** 634
[26] Cao B J, Huang C, Jiang L Z, Pan Y F, Shi D N, Fan J Y, Ma C L, and Zhu Y 2025 *Chin. Phys. Lett.* **42** 070714
[27] Yuan H, Shimotani H, Tsukazaki A, Ohtomo A, Kawasaki M, and Iwasa Y 2009 *Adv. Funct. Mater.* **19** 1046
[28] Ye J T, Inoue S, Kobayashi K, Kasahara Y, Yuan H T, Shimotani H, and Iwasa Y 2010 *Nat. Mater.* **9** 125
[29] Ye J T, Zhang Y J, Akashi R, Bahramy M S, Arita R, and Iwasa Y 2012 *Science* **338** 1193
[30] Lei B, Cui J H, Xiang Z J, Shang C, Wang N Z, Ye G J, Luo X G, Wu T, Sun Z, and Chen X H 2016 *Phys. Rev. Lett.* **116** 077002
[31] Wen C H, Xu H C, Chen C, Huang Z C, Lou X, Pu Y J, Song Q, Xie B P, Abdel-Hafiez M, Chareev D A, Vasiliev A N, Peng R, and Feng D L 2016 *Nat. Commun.* **7** 10840
[32] Nakayama K, Tsubono R, Phan G N, Nabeshima F, Shikama N, Ishikawa T, Sakishita Y, Ideta S, Tanaka K, Maeda A, Takahashi T, and Sato T 2021 *Phys. Rev. Res.* **3** L012007
[33] Zhu C S, Cui J H, Lei B, Wang N Z, Shang C, Meng F B, Ma L K, Luo X G, Wu T, Sun Z, and Chen X H 2017 *Phys. Rev. B* **95** 174513
[34] Kouno S, Sato Y, Katayama Y, Ichinose A, Asami D, Nabeshima F, Imai Y, Maeda A, and Ueno K 2018 *Sci. Rep.* **8** 14731
[35] Xu J, Qin M, Lin Z, Zhang X, Zhang R, Xu L, Zhang L, Shi Q, Yuan J, Zhu B, Dong C, Xiong R, Chen Q, Li Y, Shi J, and Jin K 2023 *Phys. Rev. B* **107** 094514
[36] Shikama N, Sakishita Y, Nabeshima F, and Maeda A 2021 *Phys. Rev. B* **104** 094512
[37] Wang W X, Lei B, Zhu C S, Cui J H, Zhuo W Z, Xiang Z J, Luo X G, and Chen X H 2022 *Phys. Rev. B* **106** 014509
[38] Jiang X Y, Qin M Y, Wei X J, Xu L, Ke J Z, Zhu H P, Zhang R Z, Zhao Z Y, Liang Q M, Wei Z X, Lin Z F, Feng Z P, Chen F C, Xiong P Y, Yuan J, Zhu B Y, Li Y M, Xi C, Wang Z, Yang M, Wang J, Xiang T, Hu J, Jiang K, Chen Q, Jin K, and Zhao Z 2023 *Nat. Phys.* **19** 365
[39] Zhang X, Feng Z, Wei X, Lin Z L, Jiang X, Hu W, Wei Z, Qin M, Xu J, Xiong R, Shi J, Yuan J, Zhu B, Chen Q, and Jin K 2021 *Phys. Rev. B* **103** 214505
[40] Liu T J, Ke X, Qian B, Hu J, Fobes D, Vehstedt E K, Pham H, Yang J H, Fang M H, Spinu L, Schiffer P, Liu Y, and Mao Z Q 2009 *Phys. Rev. B* **80** 174509
[41] Sun Y, Yamada T, Pyon S, and Tamegai T 2016 *Sci. Rep.* **6** 32290
[42] Mukasa K, Matsuura K, Qiu M, Saito M, Sugimura Y, Ishida K, Otani M, Onishi Y, Mizukami Y, Hashimoto K, Gouchi J, Kumai R, Uwatoko Y, and Shibauchi T 2021 *Nat. Commun.* **12** 381
[43] Mukasa K, Ishida K, Imajo S, Qiu M, Saito M, Matsuura K, Sugimura Y, Liu S, Uezono Y, Otsuka T, Čulo M, Kasahara S, Matsuda Y, Hussey N E, Watanabe T, Kindo K, and Shibauchi T 2023 *Phys. Rev. X* **13** 011032
[44] Ding Q P, Schmidt J, Moreno J A, Bud'ko S L, Canfield P C, and Furukawa Y 2025 *Phys. Rev. Lett.* **134** 226002
[45] Wang W, Liu Y, Yang J, Du H, Ning W, Ling L, Tong W, Qu Z, Yang Z, Tian M, and Zhang Y 2016 *Chin. Phys. Lett.* **33** 057401

[46] Li C, Song Y, Wang X, Lei M, Chen X, Xu H, Peng R, and Feng D 2024 *Nano Lett.* **24** 8303

[47] Ieki E, Nakayama K, Miyata Y, Sato T, Miao H, Xu N, Wang X P, Zhang P, Qian T, Richard P, Xu Z J, Wen J S, Gu G D, Luo H Q, Wen H H, Ding H, and Takahashi T 2014 *Phys. Rev. B* **89** 140506

[48] Lei B, Wang N Z, Shang C, Meng F B, Ma L K, Luo X G, Wu T, Sun Z, Wang Y, Jiang Z, Mao B H, Liu Z, Yu Y J, Zhang Y B, and Chen X H 2017 *Phys. Rev. B* **95** 020503

[49] Wang Q, Shen Y, Pan B, Hao Y, Ma M, Zhou F, Steffens P, Schmalzl K, Forrest T R, Abdel-Hafiez M, Chen X, Chareev D A, Vasiliev A N, Bourges P, Sidis Y, Cao H, and Zhao J 2015 *Nat. Mater.* **15** 159

[50] Wang Q, Shen Y, Pan B, Zhang X, Ikeuchi K, Iida K, Christianson A D, Walker H C, Adroja D T, Abdel-Hafiez M, Chen X, Chareev D A, Vasiliev A N, and Zhao J 2016 *Nat. Commun.* **7** 12182

[51] Liu R X, Nakamura M, Kamazawa K, and Lu X Y 2024 *Chin. Phys. Lett.* **41** 067401

[52] Liu T J, Hu J, Qian B, Fobes D, Mao Z Q, Bao W, Reehuis M, Kimber S A J, Prokeš K, Matas S, Argyriou D N, Hiess A, Rotaru A, Pham H, Spinu L, Qiu Y, Thampy V, Savici A T, Rodriguez J A, and Broholm C 2010 *Nat. Mater.* **9** 718

[53] Lumsden M D, Christianson A D, Goremychkin E A, Nagler S E, Mook H A, Stone M B, Abernathy D L, Guidi T, MacDougall G J, de la Cruz C, Sefat A S, McGuire M A, Sales B C, and Mandrus D 2010 *Nat. Phys.* **6** 182

[54] Tranquada J M, Xu G, and Zaliznyak I A 2020 *J. Phys.: Condens. Matter* **32** 374003